Ab initio Modeling of Optical Functions after Strain Wave Perturbation for Defect Detection

Sean M. Anderson,* Bernardo S. Mendoza, and Ramón Carriles

Centro de Investigaciones en Óptica, León, Guanajuato, México

(Dated: June 4, 2019)

We model the change in the linear optical functions due to the propagation of a strain wave through a crystalline slab. Defects in the slab are introduced by arbitrarily displacing one of the atomic layers. The perturbing wave is assumed to be produced by laser light absorption; the properties of the propagating wave are explicitly related to the laser and material properties. We apply this model to a Si(111)(1×1):H slab, and find that the reflectance varies significantly at photon energies above 2.5 eV, and that the disordered slab produces significant changes in the reflectance when compared to the unperturbed slab. We then induce a defect layer in the slab by uniformly translating an atomic layer. As the strain wave passes through the material, the behavior of the calculated reflectance difference spectrum changes according to the defect layer, allowing us to discern the depth of the defect.

Keywords: reflectance spectroscopy, atomic disorder, strain wave, surface, depth probing

I. INTRODUCTION

Defect characterization and profiling techniques in solid materials are becoming increasingly relevant, coinciding with the many new advances in micro- and optoelectronics. It is therefore desirable to develop techniques capable of non-destructive and *in-situ* characterization; particularly, optical methods have a strong background of applications in this area. These developments require better theoretical models to understand the experimental observations. *Ab initio* calculations have been used to obtain optical properties of materials under strain or with defects. With current computational systems the calculations from surface or bulk regions are both efficient and numerically accurate[1–6].

Experimentally, pump-probe techniques[7–11] have been widely used to measure and characterize buried defects and interfaces. In these experiments, at least two laser beams with different intensities, typically sub-picosecond in duration, are incident on the sample with a temporal delay. The more intense pump beam is used to excite the sample, while the weaker probe beam (split off from the pump beam, or an independent synchronized beam) is used to sense the effect of the pump on the material. The temporal delay is controlled with a translational stage and can be as short as a few femtoseconds.

Among these techniques, coherent acoustic phonon (CAP) spectroscopy (also known as picosecond ultrasonics) is well established. In this case, the pump is absorbed by the sample and induces a traveling strain wave that locally modifies the optical properties as it traverses the material. The probe pulse senses the induced changes and therefore provides information about the local environment inside the sample. Due to its flexibility, the CAP method has been used to study many sample attributes, such as structural properties of a wide range of materials[12–25], characterization of thin films[26,27], determination of elasto-mechanical and optical properties[15,18,20,28–31], low-frequency phonon dispersion and attenuation[32,33], roughness of buried interfaces[34], inhomogeneities in disordered films[26], doping profiles[21], lattice defects[35–38], and shear strain waves using time-resolved polarization measurements[39,40]. Recently, the development of 2-dimensional materials and membranes has introduced new challenges related to the characterization of their properties. CAP has begun to be applied to thin films and free standing membranes[41,42], magnetic nano-films[43], nanoparticles[44], and van der Waals nanolayers[45]; however, it is necessary to refine the current theoretical models to better understand how the presence of defects alters the material properties.

In a previous work[46], we presented a simple *ab initio* model to study how the displacement of a single atomic layer inside a material affected its linear optical properties. We applied the model to a Si(111)(1×1):H slab and found that the predicted reflectance changes were within the sensitivity range of lock-in techniques. In this work, we simulate the propagation of a strain wave inside a material and the related atomic displacement induced by the traveling wave, and calculate the resulting change in the dielectric function. The goal of this work is twofold: first, to develop a realistic model of strain waves, and how they perturb a given material at the atomic level; second, to apply the developed model towards the detection of buried defects or interfaces. Although our calculations are done using an analytical form of a CAP strain wave, our model is valid for any type of deformations induced in the bulk atomic positions.

This paper is organized as follows. In Sec. II, we present the relevant equations and theory that characterize both the strain wave and the reflectance difference spectrum. In Sec. III, we present and analyze the calculated reflectance from probing a Si(111)(1×1):H surface as a test case, exploring several cases including buried defects. Finally, we list our conclusions and final remarks in Sec. IV.

II. THEORY

A. Strain wave generation from CAP pulses

We previously developed a simple proof-of-concept model[46] where individual atomic layers were uniformly translated up or down by a given percentage. These movements yielded a clear difference in reflectivity between the perturbed and unperturbed slabs, with discernible changes when either diagonal or vertical bonds underwent the deformation; specifically, elongation of the diagonal bonds (compression of the vertical bonds) leads to an increase in the reflectance difference spectrum.

Our goal is now to extend and improve upon our previous work, and create a far more realistic strain wave model that is capable of detecting defects within a given slab. As a starting point, Ref. 47 extends upon previously developed analytical models for strain wave generation from CAP[8], and demonstrates that the electronic stress plays a large role in inciting the CAP pulse. The produced strain in the z direction, η_{zz}, can be approximated in simple analytical form as[47]

$$\eta_{zz}(z,t) = -Ae^{-\alpha|z-v_st|}\,\mathrm{sgn}(z-v_st), \qquad (1)$$

where α is the absorption coefficient of the material at the pump beam energy, and v_s is the longitudinal sound velocity. The dimensionless pre-factor A determines the strength of the strain wave and is given by

$$A = \frac{\alpha(1-R_{\mathrm{pump}})Q}{2E_{\mathrm{pump}}\rho v_s^2}\left[-(d_c+d_v)\right.$$
$$\left.+\frac{3B\beta}{C_V}\left(E_{\mathrm{pump}}-E_g\right)\right], \qquad (2)$$

where R_{pump}, Q, and E_{pump} are the reflectance, fluence, and photon energy of the pump beam, E_g is the band gap energy, ρ is the mass density, d_c and d_v are the electron and hole deformation potentials, B is the bulk modulus, β is the linear thermal expansion coefficient, and C_V is the specific heat per unit volume. The produced strain in Eq. (1) is related to the lattice displacement $u(z,t)$ as

$$\eta_{zz}(z,t) = \frac{\partial u(z,t)}{\partial z};$$

after integrating with respect to z, we finally obtain

$$u(z,t) = -\frac{A}{2\alpha}\left(e^{\alpha(-z+v_st)}\left[\mathrm{sgn}(-z+v_st)-1\right]\right.$$
$$\left.+e^{\alpha(+z-v_st)}\left[\mathrm{sgn}(+z-v_st)-1\right]\right). \qquad (3)$$

Fig. 1 depicts the calculated strain and displacement profiles obtained from Eqs. (1) and (3) for a fixed time t as functions of the distance traveled, into the material, $z-v_st$. These curves are produced using physical parameters for silicon (see Tables I and II). As the pulse travels through the material, the atoms will be displaced
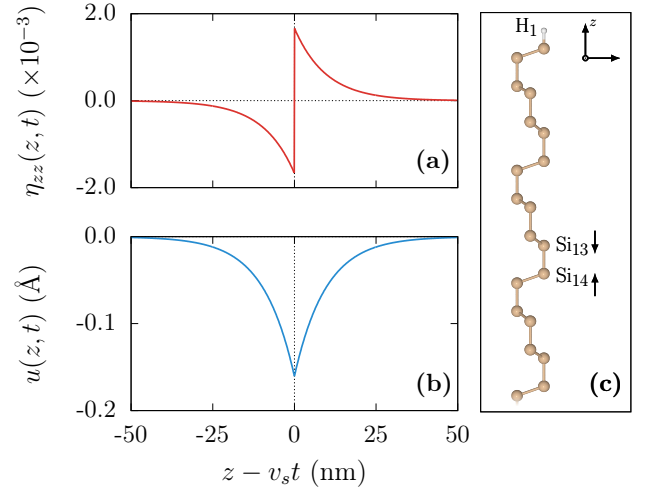

FIG. 1. Time-snapshot of the (a) strain and (b) displacement profiles (as functions of the distance traveled) of a CAP pulse using parameters for silicon (Tables I and II). These plots were calculated for a fluence $Q = 0.3\,\mathrm{mJ/cm}^2$, a pump photon energy $E_{\mathrm{pump}} = 3.54\,\mathrm{eV}$ which corresponds to an absorption coefficient $\alpha = 1.04\times10^6\,\mathrm{cm}^{-2}$. (c) Cartoon representation of the slab unit cell, with two Si labeled atoms that will be moved in the direction indicated to create buried defect layers. The x and y axes are taken along the $[11\bar{2}]$ and $[1\bar{1}0]$ directions, respectively.

according to Eq. (3); thus, careful selection of the beam characteristics will greatly affect how much the (and how many) atoms are displaced from their equilibrium positions.

B. *Ab initio* calculation of the reflectance

To model a semi-infinite crystal, we create a slab consisting of N atomic layers and thickness D inside of a super-cell of height L; this super-cell includes a vacuum region that is large enough to avoid spurious wavefunction tunneling into neighboring super-cells[4]. The slab surface is parallel to the xy plane. The reflectance differ-

TABLE I. Material constants for silicon.

Parameter	Sym.	Value
Longitudinal sound velocity	v_s	$8433\,\mathrm{m\,s}^{-1}$[48]
Mass density	ρ	$2.3296\,\mathrm{g\,cm}^{-3}$
Bulk modulus	B	$98\,\mathrm{GPa}$[49]
Thermal expansion coefficient	β	$2.56\times10^{-6}\,\mathrm{K}^{-1}$
Electron deformation potential	d_c	$9.5\,\mathrm{eV}$[50]
Hole deformation potential	d_v	$5.0\,\mathrm{eV}$[50]
Direct Band gap	E_g	$3.4\,\mathrm{eV}$[51]
Specific heat per unit volume	C_V	$1.63072\,\mathrm{J\,cm}^{-3}\,\mathrm{K}^{-1}$

TABLE II. Beam and wavelength-dependent parameters used throughout this work, unless stated otherwise.

Parameter	Sym.	Value
Pump beam fluence	Q	$0.5861\,\mathrm{mJ\,cm^{-2}}$
Pump beam energy	E_{pump}	$3.54\,\mathrm{eV}$
Pump beam reflectance	R_{pump}	0.56538
Pump beam absorption	α	$1.04 \times 10^{-6}\,\mathrm{cm^{-1}}$

ence spectrum ΔR is defined as[4]

$$\Delta R = \left.\frac{R_x + R_y}{2}\right|_{\mathrm{unperturbed}} - \left.\frac{R_x + R_y}{2}\right|_{\mathrm{perturbed}},$$

where R_{a} ($\mathrm{a} = x$ or y) is the normal incident reflectance for linearly polarized light in the $\hat{\mathbf{a}}$ direction. As explained above, the advancing strain wave will displace the atoms of the slab away from their equilibrium positions; we calculate R_{a} for this perturbed slab and obtain the difference (ΔR) between the reflectance of the perturbed and unperturbed slabs. R_{a} can be calculated through the optical response of the slab system[52] as

$$R_{\mathrm{a}} = 4\left(\frac{\omega}{c}\right)\mathrm{Im}\left[\frac{(D/2)\chi_{sc}^{\mathrm{aa}}(\omega)}{\boldsymbol{\chi}_b(\omega)}\right], \qquad (4)$$

where ω is the angular frequency of the normally incident light impinging at the slab surface, c is the speed of light, $D/2$ is half of the slab thickness, $\boldsymbol{\chi}_{sc}(\omega)$ is the linear susceptibility for the supercell system, and $\boldsymbol{\chi}_b(\omega)$ is the linear susceptibility of the isotropic bulk crystal.

The linear susceptibility tensor is calculated within the independent-particle framework as

$$\chi^{\mathrm{aa}}(\omega) = \frac{e^2}{\hbar}\int\frac{d\mathbf{k}}{8\pi^3}\sum_{m<n}\frac{2f_{mn}(\mathbf{k})}{W_{nm}(\omega)}\mathrm{Im}\left[v_{nm}^{\mathrm{a}}(\mathbf{k})r_{mn}^{\mathrm{a}}(\mathbf{k})\right], \qquad (5)$$

where $v_{nm}^{\mathrm{a}}(\mathbf{k})$ and $r_{nm}^{\mathrm{a}}(\mathbf{k})$ are the matrix elements of the electron velocity and position operators, with a, b $= x, y$ and n, m represent the electronic bands. The Fermi-Dirac distribution is represented as a Heaviside function, $f_n(\mathbf{k}) = \Theta\left(E_F - E_n(\mathbf{k})\right)$, where E_F is the Fermi energy, $E_n = \hbar\omega_n(\mathbf{k})$ is the energy of the electronic band n at point $\mathbf{k}$ in the irreducible Brillouin zone, and $f_{mn}(\mathbf{k}) = f_m(\mathbf{k}) - f_n(\mathbf{k})$. Lastly, we have

$$W_{nm}(\omega) = (\omega_{nm} - \omega - i\gamma)(\omega_{nm} + \omega + i\gamma),$$

where $\omega_{nm}(\mathbf{k}) = \omega_n(\mathbf{k}) - \omega_m(\mathbf{k})$. Many-body interactions can be included in $\omega_{nm}(\mathbf{k})$ by making use of the scissors operator. The first (second) term includes the resonant (nonresonant) terms. γ signifies the adiabatic switching of the interaction, and can also be used to include the broadening of the electronic levels. The limit of $\gamma \to 0$ leads to the Dirac delta functions $\delta(\omega_{nm}(\mathbf{k}) - \omega)$ for the resonant term, and $\delta(\omega_{nm}(\mathbf{k}) + \omega)$ for the nonresonant term; both are needed to accurately calculate $\chi^{\mathrm{aa}}(\omega)$[53].

The bulk susceptibility, $\boldsymbol{\chi}_b(\omega)$, is obtained by using a bulk unit cell in Eq. (5); likewise, $\boldsymbol{\chi}_{sc}(\omega)$ is obtained by using a supercell, where it must be properly normalized with respect to the vacuum included in the total supercell height L[54]. Then, we take $\boldsymbol{\chi}_{sc}(\omega) \to (L/D)\boldsymbol{\chi}_{sc}(\omega)$, so that even if a larger vacuum region is included, the results remains invariant.

C. Test Case, Computational Details, and Depth probing

We carry out our study using the Si(111)(1×1):H surface, where the addition of an H atom at each surface passivates the dangling bond of the ideal Si(111) bulk and yields an unreconstructed surface with a 1×1 unit cell. In this work, our surface is represented by a centrosymmetric slab of 98 atomic layers comprised of 96 Si atoms between two H atoms, one at each surface; the total height of this slab is 151 Å. This number of atoms results in a total of 193 occupied states (neglecting spin); we can fully describe the desired spectral energy range by including 107 unoccupied states. The hexagonal symmetry of this surface is such that $\chi_{sc}^{xx}(\omega) = \chi_{sc}^{yy}(\omega)$, and thus $R_x = R_y$.

The self-consistent ground state and the Kohn-Sham states needed to construct the electron velocity and position matrix elements in Eq. (5), were calculated within the DFT-LDA framework using the plane-wave ABINIT code[55,56] using a planewave basis set with Troullier-Martin LDA pseudopotentials[57]. Our calculation of $\chi_{sc}^{aa}(\omega)$ was carried out using the TINIBA code[58]. We found converged results with 91 $\mathbf{k}$-points in the irreducible Brillouin zone (equivalent to 1922 $\mathbf{k}$-points when neglecting symmetry relations) and an energy cutoff of 7 Hartrees. Likewise, 3107 $\mathbf{k}$ points and a cutoff energy of 10 Ha were used for the bulk $\boldsymbol{\chi}_b(\omega)$ calculation. A scissors shift of 0.7 eV was used for both the surface and bulk susceptibilities featured in Eq. (4), obtained from *ab initio* G_0W_0 calculations[59]. The contribution from the nonlocal part of the pseudopotentials[60] was carried out using the DP[61,62] code with a basis set of 5000 planewaves.

Eqs. (2) and (3) establish how the physical parameters of the material, in conjunction with the pump beam properties, are responsible for determining the strain wave displacement amplitude and width. Some of these parameters are constants that are specific to the material; for instance, see Table I for a summary of the physical constants for silicon. Parameters such as E_{pump} and Q are determined solely by the laser system, while α and R_{pump} are both material-specific and wavelength-dependent. This gives us flexibility to select the best parameters for modeling a realistic strain wave that is well-suited for our sample slab (with the necessary computational expense), while using real-world beam characteristics that can be found in many modern ultrafast laser systems. Table II summarizes the beam and wavelength-dependent parameters we used throughout this work, un-

less stated otherwise.

After selecting the appropriate constants and parameters, we simulate the traveling strain wave by calculating the atomic displacement from Eq. (3). The maximum displacement wave-front travels through the slab (localized at $v_s t$), and the atoms are displaced by the corresponding amount depending on their distance from the wave-front. In order to minimize the computation expense, we executed a calculation with the wave-front centered at the z-coordinate of each atomic layer. Therefore, each result presented below consists of 98 separate calculations, one for each step in the strain wave's movement through the slab. It is important to note that the constants and parameters from Tables I and II produce a strain wave that is wider than our 151 Å-deep slab; however, as we are mostly interested in the defect-probing capabilities, the small size of the slab is not a limitation.

III. RESULTS

In this section, we will review our calculated results for ΔR generated by perturbing the Si(111)(1×1):H test slab with a strain wave generated with the parameters from Tables I and II. We will consider the upper slab surface at $z = 0$, and the bottom surface at $z = 151$ Å; while this size is several orders of magnitude smaller than the samples used in most CAP experiments[35,36,63,64], we are still able to gain insight on the microscopic perturbations that lead to significant changes in the reflectance difference spectrum.

Fig. 2, panel (a) presents ΔR generated by the CAP pulse at the top surface of the slab ($z = 0$) for maximum displacement values of 0.313, 0.235, and 0.157 Å, which represent 40, 30, and 20 % of the diagonal bond height $H_d = 0.784$ Å. These displacements are generated using fluence values of $Q = 0.586$, 0.440 and 0.293 mJ cm^{-2}, respectively, and are of the same order as those induced in real samples during a CAP experiment[64], and are large enough to create clear features in the spectrum, without creating spurious effects from overly distorted atomic positions. We can see that ΔR changes monotonically with the fluence; as the fluence is only limited by the damage threshold of the sample material, we can essentially select any realistic value that yields desirable pulse characteristics. Thus, we will use $Q = 0.586$ mJ cm^{-2} (max. displacement of 40 % H_d) for the remainder of this work.

Given that the strain pulse is capable of generating a significant change in the reflectance, we are now ready to analyze the effect of defects and buried interfaces on the spectrum. Fig. 2, panel (b) presents ΔR generated by the strain wave wave-front at the top-most surface atom of a variety of slabs, with and without defect layers. To identify which atom will be moved to create a defect layer, we tag each one in consecutive order starting at the surface, i.e. H_1 and Si_2 down to Si_{97} and H_{98}. Odd Si atoms have the vertical bonds going down and the slanted bonds going up, and vice versa for the even Si atoms; see

Fig. 1, panel (c) for a cartoon representation of the slab. We create the defect layers by moving a given atom up or down by 0.313 Å (40 % of H_d); Si_{13} is moved downwards, while Si_{14}, Si_{26}, and Si_{50} are moved upwards. The curve labeled "None" (black solid line) is the slab without any defect, the same shown in panel (a).

Between 3.0–5.0 eV, ΔR remains quite similar between the normal and defective slabs. The spectra is dominated by 2 peaks at around ~3.4 eV and ~4.3 eV, which correspond to the E_1 and E_2 critical points of silicon, with a smaller feature around 4.0 eV. These peaks mostly retain their position despite the presence of the defect layers, with small variations in the peak height. The most interesting feature of the spectra occurs in 2.5–3.0 eV energy range, highlighted in the dashed box. A small peak emerges for the defective slabs that is completely absent from the spectra of the normal slab. The height of this peak is larger for slabs with the defect layer closer to the upper surface; likewise, the peak energy position also shifts slightly from higher energies to lower energies in the same manner. For convenience of notation, we will call this the defect peak.

To explore the depth-probing effects of the strain wave, and the nature of the defect peak, in Fig. 3 we present two three-dimensional representations of ΔR as the strain wave travels through the slab. First, Fig. 3a shows the wave traveling through the normal slab without defects. ΔR starts at its maximum value as the wave-
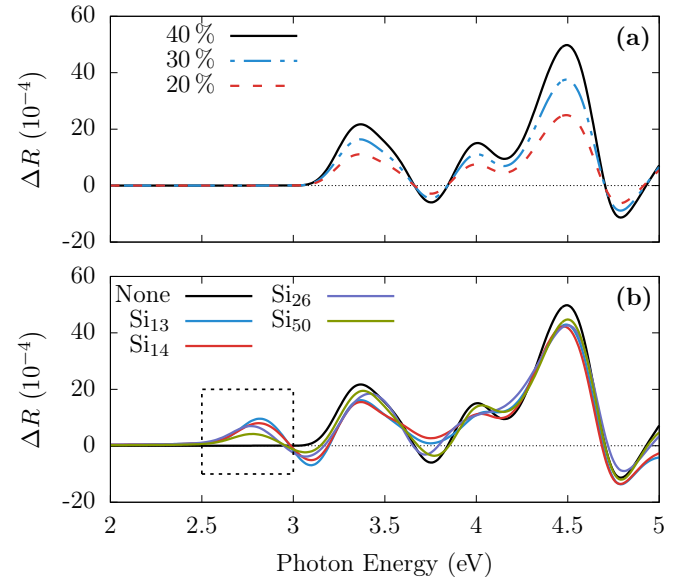

FIG. 2. **(a)** ΔR for maximum displacements of 40, 30, and 20 % of the diagonal bond height $H_d = 0.784$ Å, generated with three different fluence values ($Q = 0.586$, 0.440 and 0.293 mJ cm^{-2}). **(b)** ΔR calculated from a max. displacement of 40 % of H_d for the normal slab and five cases of slabs with defect layers at the atom indicated in the label for each curve; all curves are produced when the strain maximum (the wave-front) is at the top surface of the material. The dashed box highlights the defect peak.
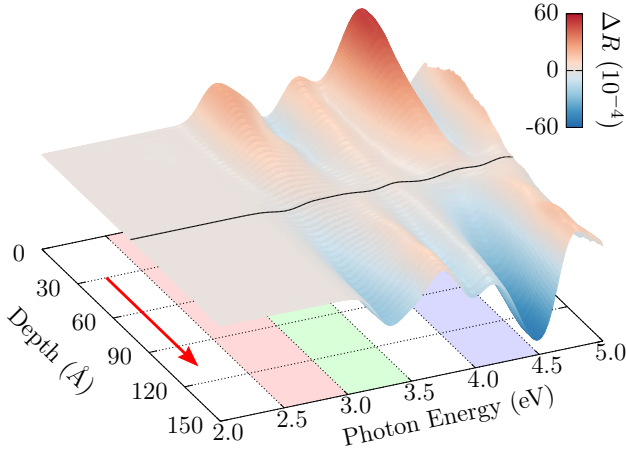
(a) Strain wave traveling through a slab with no defect. ΔR goes from maximum to minimum, passing through zero at the middle of the slab. The thin black line indicates the center of the slab at which ΔR is at a minimum.
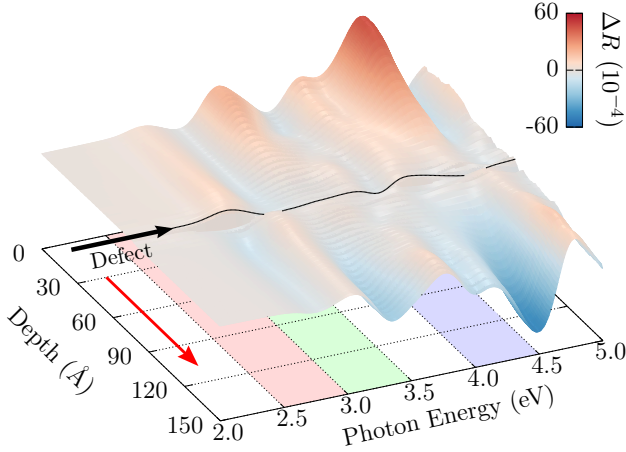
(b) Strain wave traveling through a slab with a defect layer at atom Si_{50}. The defect peak goes from positive to negative at the exact position of the defect layer. The thin black line is a visual aid indicating the depth at which change in ΔR occurs due to the defect layer.

FIG. 3. Three-dimensional representation of the reflectivity difference spectrum (ΔR) as a function of the strain wave depth inside the slab. The red arrow indicates the direction of propagation of the wave, starting at a depth of 0 (top surface of the slab) to 151 Å (bottom surface of the slab). Colored energy regions will be referred to below.

front is located at the material surface. At the middle of the slab, ΔR essentially goes to zero; after this point, ΔR goes to negative values, inverting the shape from the upper half of the slab. This behavior is due to the fact that our Si(111)(1×1):H slab is centrosymmetric; as the wave reaches the middle of the slab, the strain wave deforms the upper half in almost exactly the same way as the lower half. The changes in the reflectance from the upper half cancel out those from the lower half, and thus ΔR mostly vanishes. As shown previously in Fig. 2, the region between 2.5–3.0 eV is devoid of any activity.

Second, Fig. 3b presents the same representation for

a slab with a defect layer present at atom Si_{50}, indicated by the black arrow. The general behavior is similar to the normal slab from Fig. 3a; however, the defect peak suffers a very marked sign change, from positive to negative, at the exact position of the defect layer. In fact, we can see a disturbance across the entire energy range when reaching the defect layer. This behavior remains consistent for the other defective slabs listed in Fig. 2. The colored regions on the grid below the plot highlight three energy ranges; light red for 2.5–3.0 eV, light green for 3.0–3.5 eV, and light purple for 4.0–4.5 eV, representing the defect peak, the E_1 peak, and the E_2 peak, respectively. In order to better analyze the changes to ΔR in the presence of the defect layers, we will study the peaks located in each of these energy ranges separately.

We present the aforementioned peak analysis in Fig. 4, where we plot the intensity of each peak as a function of the strain wave depth within the slab. Panel (a) depicts the defect peak behavior in the 2.5–3.0 eV range (light red region from Fig. 3), panel (b) for the E_1 peak in the 3.0–3.5 eV range (light green region), and the E_2 peak in the 4.0–4.5 eV range (light purple region). We can now clearly see the behavior of the defect peak for the different defective slabs; when the strain wave reaches a defect layer, the defect peak goes from positive to negative. The peak amplitude remains negative after the inversion, and for the remainder of the strain wave's course through the slab. Therefore, in order to elucidate the defect layer depth, the measurement would only have to be taken over the 2.5–3.0 eV energy range, and when the ΔR signal has an abrupt sign change, we know that the strain wave has reached the defect layer.

Following the same analysis for the E_1 and E_2 peaks (panels (b) and (c)), we see that the induced behavior is not nearly as obvious as for the defect peak. For the slab with the Si_{26} defect layer, there is a small dip in the intensity occurring for both peaks before the reaching the defect layer. Likewise, both peaks have a similar amplitude dip for the Si_{13} and Si_{14} defective slabs. Interestingly, the places where amplitude of the E_1 peak from the defective slabs crosses over the curve representing the normal slab (black curve) is quite close to the actual defect layer locations. In other words, the magnitude of the E_1 peak increases after a defect layer, when compared directly to the same peak produced in the normal slab. However, this difference is relatively small and may not be distinct enough to be measured; also, this behavior is not as strictly followed for the E_2 peak. Lastly, the slab with the Si_{50} defect layer follows similar trends, but since the defect is located at the very center of the slab, the changes are more gradual and are quite close to the normal slab. However, the inflection point of the curve does indeed indicate the exact location of the defect layer.

These results are consistent with our previous work[46]. In particular, defect layers leading to elongated diagonal bonds (corresponding to upward displacement of even Si atoms, or downward displacement of odd Si atoms) yield an increase in ΔR precisely around the same energy en-
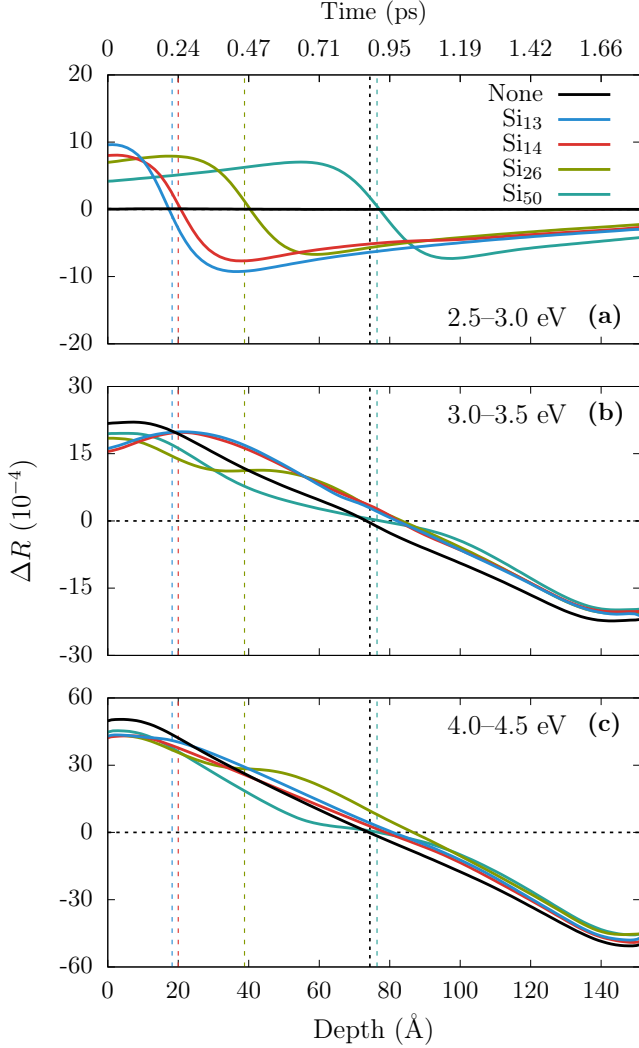
FIG. 4. Peak behavior for the normal and defective slabs, over the **(a)** 2.5–3.0 eV, **(b)** 3.0–3.5 eV, and **(c)** 4.0–4.5 eV regions. These correspond to the light red, light green, and light purple regions from Fig. 3, respectively. Thin vertical colored dashed lines indicate the defect depth within the slab. The thick black vertical dashed line represents the middle of the slab.

ergy range (> 2.5 eV) as the defect peak reported here. If we consider the response of the bonds as linear harmonic oscillators, an electron in an elongated bond will have a looser confinement compared to a compressed bond. The electron potential for the elongated bond will have a lower curvature, implying that the resonant frequency (proportional to the curvature) will be lower; thus, the elongated bond has a higher polarizability which leads to a larger ΔR.

We can further our understanding of these results from a different perspective, by calculating the dimensionless planar-integrated electron density[4],

$$\rho_{n\mathbf{k}}(z) = L \int |\psi_{n\mathbf{k}}(\mathbf{r})|^2 \, dx \, dy,$$

for the nth valence band and $\mathbf{k}$-vector that contribute to a given resonance in χ^{aa} that originates the peaks in ΔR. L is the total height of the slab, from top surface to bottom surface. For the slab with a defect at Si_{13}, the defect peak at 2.8 eV (dashed box in panel (b) of Fig. 2) corresponds to $\mathbf{k} = (0.032\,\hat{x} + 0.055\,\hat{y})\,\text{Å}^{-1}$. Likewise, we can analyze the peak at 4.4 eV for the relaxed slab (no defect) that corresponds to $\mathbf{k} = (0.062\,\hat{x} + 0.110\,\hat{y})\,\text{Å}^{-1}$. For both the relaxed and defective slabs, $n = 193$ which corresponds to the topmost valence band.

Using the aforementioned values, we present the electron density as a function of depth in Fig. 5. We see that for the relaxed structure, $\rho_{n\mathbf{k}}(z)$ is a periodic, symmetric function that grows towards the center of the slab, which is consistent with the ordered and centrosymmetric nature of the atomic structure. The maxima of the electron density are centered at the Si atomic positions. Conversely, the electron density for the Si_{13} defect structure shows a very intense peak that is highly localized at the position of the Si_{13} atom. In this case, the strain wave maximum is also centered on this atom, thus displacing it the maximum amount away from its relaxed position. We conducted a similar analysis for the other peaks around 2.8 eV produced from the Si_{14}, Si_{26}, Si_{50} defect slabs, and the electron density yields an analogous intense peak at the corresponding defect z-positions. Therefore, the peaks in ΔR around 2.8 eV shown in panel (b) of Fig. 2 come from very localized defect states induced by the strain wave.

Our results clearly show that the calculated signals are well within the detection range of lock-in techniques; thus, depth-probing and defect detection should be possible with this method. Experimentally, it is not easy to obtain a sample as the ones described above. However, a feasible test material could be synthesized with a buried monolayer comprised of some other material, in lieu of having a layer of atoms displaced from their equilibrium position. We emphasize that even though the specifics
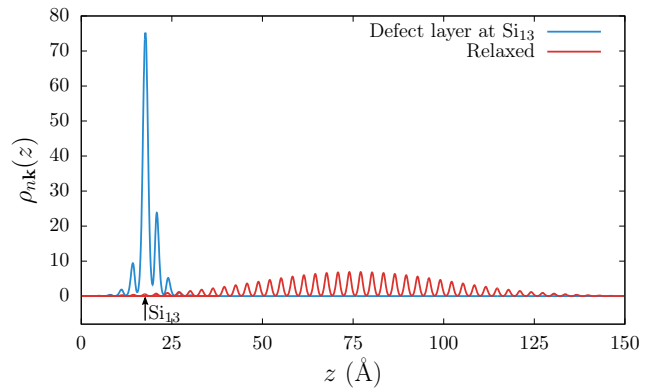

FIG. 5. The planar-integrated electron density $\rho_{n\mathbf{k}}(z)$ as a function of depth for the relaxed slab and the defective slab with a defect layer at Si_{13}. The small black arrow indicates the z position of Si_{13}.

of our results depend on the excitation, the model can be applied to an arbitrary perturbation that produces a strain wave, and is not necessarily exclusive to CAP experiments. Although the type of defect layer presented here (created via uniform atomic displacement) would be difficult to recreate experimentally, it provides an effective test platform for our method. Localized defects, such as those produced by doping, require very large unit cells that increase the computational demand of the calculations. As is, our method should be effective at discovering buried interfaces, even between different materials.

IV. CONCLUSIONS

Overall, our method for modeling the atomic displacement in a crystalline slab induced by an advancing strain wave proves to be effective at discerning buried defect layers. The strain wave is obtained by using realistic material constants and beam parameters; thus, the atomic displacement is an accurate representation of what might occur with a strain wave from a CAP experiment. The calculated difference reflectance spectrum for our Si(111)(1×1):H test system yields a unique peak in the 2.5–3.0 eV energy range that acts as a defect signature, allowing us to accurately pinpoint the defect layer depth.

Although the model presented here is a significant advancement over our previous work[46] due to the more accurate representation of the strain wave, we have yet to incorporate the interference effects that occur as the probe light enters the material and interacts with the strain wave, and undergoes multiple reflections before exiting the material. This would require either a much larger slab, so that the atoms displaced by the strain wave could be more localized, or the use of another material with constants that lead to a much narrower strain wave. Larger slabs lead to significantly larger computational expense; therefore, we consider that there may be other materials that could produce very localized strain waves, where the disordered region can be clearly isolated from the remainder of the unperturbed material. The development of such a model would essentially complete our proposed *ab initio* description of CAP spectroscopy, and should be achievable in the near future.

V. ACKNOWLEDGEMENTS

[*] sma@cio.mx

[1] C. D. Hogan and C. H. Patterson, Phys. Rev. B **57**, 14843 (1998).

[2] M. Palummo, G. Onida, R. Del Sole, and B. S. Mendoza, Phys. Rev. B **60**, 2522 (1999).

[3] C. Hogan, R. Del Sole, and G. Onida, Phys. Rev. B **68**, 035405 (2003).

[4] B. S. Mendoza, F. Nastos, N. Arzate, and J. E. Sipe, Phys. Rev. B **74**, 075318 (2006).

[5] M. Palummo, N. Witkowski, O. Pluchery, R. Del Sole, and Y. Borensztein, Phys. Rev. B **79**, 035327 (2009).

[6] K. Hingerl, R. E. Balderas-Navarro, A. Bonanni, P. Tichopadek, and W. G. Schmidt, Appl. Surf. Sci. **175-176**, 769 (2001).

[7] C. H. Thomsen, J. Strait, Z. Vardeny, H. J. Maris, J. Tauc, and J. J. Hauser, Phys. Rev. Lett. **53**, 989 (1984).

[8] C. H. Thomsen, H. T. Grahn, H. J. Maris, and J. Tauc, Phys. Rev. B **34**, 4129 (1986).

[9] H. T. Grahn, H. J. Maris, and J. Tauc, IEEE J. Quant. Electron. **25**, 2562 (1989).

[10] H.-N. Lin, R. J. Stoner, H. J. Maris, and J. Tauc, J. Appl. Phys. **69**, 3816 (1991).

[11] T. Pfeifer, W. Kütt, H. Kurz, and R. Scholz, Phys. Rev. Lett. **69**, 3248 (1992).

[12] D. Lim, R. D. Averitt, J. Demsar, A. J. Taylor, N. Hur, and S. W. Cheong, Appl. Phys. Lett. **83**, 4800 (2003).

[13] I. Bozovic, M. Schneider, Y. Xu, R. Sobolewski, Y. H. Ren, G. Lüpke, J. Demsar, A. J. Taylor, and M. Onellion, Phys. Rev. B **69**, 132503 (2004).

[14] O. Matsuda, O. B. Wright, D. H. Hurley, V. E. Gusev, and K. Shimizu, Phys. Rev. Lett. **93**, 095501 (2004).

[15] C. Rossignol, J. M. Rampnoux, M. Perton, B. Audoin, and S. Dilhaire, Phys. Rev. Lett. **94**, 166106 (2005).

[16] H. Park, X. Wang, S. Nie, R. Clinite, and J. Cao, Phys. Rev. B **72**, 100301(R) (2005).

[17] S. Wu, P. Geiser, J. Jun, J. Karpinski, J.-R. Park, and R. Sobolewski, Appl. Phys. Lett. **88**, 041917 (2006).

[18] J. K. Miller, J. Qi, Y. Xu, Y.-J. Cho, X. Liu, J. K. Furdyna, I. Perakis, T. V. Shahbazyan, and N. H. Tolk, Phys. Rev. B **74**, 113313 (2006).

[19] Y.-C. Wen, L.-C. Chou, H.-H. Lin, V. Gusev, K.-H. Lin, and C.-K. Sun, Appl. Phys. Lett. **90**, 172102 (2007).

[20] Y. Xu, J. Qi, J. Miller, Y.-J. Cho, X. Liu, J. K. Furdyna, T. V. Shahbazyan, and N. H. Tolk, Phys. Status Solidi B **5**, 2632 (2008).

[21] F. Hudert, A. Bartels, T. Dekorsy, and K. Köhler, J. Appl. Phys. **104**, 123509 (2008).

[22] P. Ruello, S. Zhang, P. Laffez, B. Perrin, and V. Gusev, Phys. Rev. B **79**, 094303 (2009).

[23] P. Babilotte, P. Ruello, D. Mounier, T. Pezeril, G. Vaudel, M. Edely, J.-M. Breteau, V. Gusev, and K. Blary, Phys. Rev. B **81**, 245207 (2010).

[24] P. Ruello, T. Pezeril, S. Avanesyan, G. Vaudel, V. Gusev, I. C. Infante, and B. Dkhil, Appl. Phys. Lett. **100**, 212906 (2012).

[25] L. Y. Chen, J. C. Yang, C. W. Luo, C. W. Laing, K. H. Wu, J.-Y. Lin, T. M. Uen, J. Y. Juang, Y. H. Chu, and T. Kobayashi, Appl. Phys. Lett. **101**, 041902 (2012).

[26] V. Gusev, A. M. Lomonosov, P. Ruello, A. Ayouch, and G. Vaudel, J. Appl. Phys. **110**, 124908 (2011).

[27] O. Matsuda and O. B. Wright, J. Opt. Soc. Am. B **19**, 3028 (2002).

[28] H. T. Grahn, D. A. Young, H. J. Maris, J. Tauc, J. M. Hong, and T. P. Smith, Appl. Phys. Lett. **53**, 2023 (1988).

[29] H. T. Grahn, H. J. Maris, J. Tauc, and K. S. Hatton, Appl. Phys. Lett. **53**, 2281 (1988).

[30] H. Tanei, N. Nakamura, H. Ogi, M. Hirao, and R. Ikeda, Phys. Rev. Lett. **100**, 016804 (2008).

[31] J. Qi, J. A. Yan, H. Park, A. Steigerwald, Y. Xu, S. N. Gilbert, X. Liu, J. K. Furdyna, S. T. Pantelides, and N. H. Tolk, Phys. Rev. B **81**, 115208 (2010).

[32] T. C. Zhu, H. J. Maris, and J. Tauc, Phys. Rev. B **44**, 4281 (1991).

[33] B. C. Daly, K. Kang, Y. Wang, and D. G. Cahill, Phys. Rev. B **80**, 174112 (2009).

[34] G. Tas, J. J. Loomis, H. J. Maris, A. A. Bailes, and L. E. Seiberling, Appl. Phys. Lett. **72**, 2235 (1998).

[35] A. Steigerwald, A. B. Hmelo, K. Varga, L. C. Feldman, and N. H. Tolk, J. Appl. Phys. **112**, 013514 (2012).

[36] A. Steigerwald, Y. Xu, J. Qi, J. Gregory, X. Liu, J. K. Furdyna, K. Varga, A. B. Hmelo, G. Lüpke, L. C. Feldman, and N. H. Tolk, Appl. Phys. Lett. **94**, 111910 (2009).

[37] J. Gregory, A. Steigerwald, H. Takahashi, A. Hmelo, and N. H. Tolk, Appl. Phys. Lett. **101**, 181904 (2012).

[38] A. Baydin, H. Krzyzanowska, M. Dhanunjaya, S. V. S. Nageswara Rao, J. L. Davidson, L. C. Feldman, and N. H. Tolk, APL Photonics **1**, 036102 (2016).

[39] D. Mounier, E. Morozov, P. Ruello, J.-M. Breteau, P. Picart, and V. Gusev, Eur. Phys. J. Spec. Top. **153**, 243 (2008).

[40] D. Mounier, P. Picart, P. Babilotte, P. Ruello, J.-M. Breteau, T. Pézeril, G. Vaudel, M. Kouyaté, and V. Gusev, Opt. Express **18**, 6767 (2010).

[41] J.-H. Lin, Y.-K. Shen, W.-R. Liu, C.-H. Lu, Y.-H. Chen, C. Chang, W.-C. Lee, M. Hong, J.-R. Kwo, C.-H. Hsu, and W.-F. Hsieh, J. Phys. D: Appl. Phys. **49**, 325102 (2016).

[42] C. He, O. Ristow, M. Grossmann, D. Brick, Y. Guo, M. Schubert, M. Hettich, V. Gusev, and T. Dekorsy, Phys. Rev. B **95**, 184302 (2017).

[43] T. L. Linnik, V. N. Kats, J. Jäger, A. S. Salasyuk, D. R. Yakovlev, A. W. Rushforth, A. V. Akimov, A. M. Kalashnikova, M. Bayer, and A. V. Scherbakov, Physica Scripta **92**, 054006 (2017).

[44] E. Baldini, T. Palmieri, A. Dominguez, P. Ruello, A. Rubio, and M. Chergui, Nano Lett. **18**, 5007 (2018).

[45] J. D. G. Greener, A. V. Akimov, V. E. Gusev, Z. R. Kudrynskyi, P. H. Beton, Z. D. Kovalyuk, T. Taniguchi, K. Watanabe, A. J. Kent, and A. Patanè, Phys. Rev. B **98**, 075408 (2018).

[46] S. M. Anderson, B. S. Mendoza, and R. Carriles, Phys. Status Solidi B **255**, 1700487 (2018).

[47] S. Wu, P. Geiser, J. Jun, J. Karpinski, and R. Sobolewski, Phys. Rev. B **76**, 085210 (2007).

[48] in Group IV Elements, IV-IV and III-V Compounds. Part a - Lattice Properties (Springer-Verlag) pp. 1–7.

[49] M. A. Hopcroft, W. D. Nix, and T. W. Kenny, J. Microelectromech. Syst. **19**, 229 (2010).

[50] M. Lundstrom, Fundamentals of Carrier Transport (Cambridge University Press, 2000).

[51] H. Landolt, R. Börnstein, K. H. Hellwege, J. B. Goodenough, M. Schulz, H. Weiss, and O. Madelung, Numerical data and functional relationships in science and technology, New Series: Group III, Crystal and Solid State Physics, Vol. 17, Semiconductors (Springer, Berlin, 1984).

[52] R. Del Sole, in Photonic Probes of Surfaces, Electromagnetic waves No. 2, edited by P. Halevi (Elsevier, Amsterdam; New York, 1995) pp. 131–174.

[53] N. Tancogne-Dejean, B. S. Mendoza, and V. Véniard, Phys. Rev. B **90**, 035212 (2014).

[54] N. Tancogne-Dejean, C. Giorgetti, and V. Véniard, Phys. Rev. B **92**, 245308 (2015).

[55] X. Gonze, B. Amadon, P.-M. Anglade, J.-M. Beuken, F. Bottin, P. Boulanger, F. Bruneval, D. Caliste, R. Caracas, M. Côté, T. Deutsch, L. Genovese, P. Ghosez, M. Giantomassi, S. Goedecker, D. R. Hamann, P. Hermet, F. Jollet, G. Jomard, S. Leroux, M. Mancini, S. Mazevet, M. J. T. Oliveira, G. Onida, Y. Pouillon, T. Rangel, G.-M. Rignanese, D. Sangalli, R. Shaltaf, M. Torrent, M. J. Verstraete, G. Zerah, and J. W. Zwanziger, Comp. Phys. Commun. **180**, 2582 (2009).

[56] The ABINIT code is a common project of the Université Catholique de Louvain, Corning Incorporated, and other contributors (URL http://www.abinit.org).

[57] N. Troullier and J. L. Martins, Phys. Rev. B **43**, 1993 (1991).

[58] B. S. Mendoza, S. M. Anderson, J. L. Cabellos, and T. Rangel, "TINIBA: Ab initio calculation of the optical properties of solids, surfaces, interfaces, and 2D materials," INDAUTOR-Mexico No. 03-2009-120114033400-01.

[59] Y. Li and G. Galli, Phys. Rev. B **82**, 045321 (2010).

[60] S. M. Anderson, N. Tancogne-Dejean, B. S. Mendoza, and V. Véniard, Phys. Rev. B **91**, 075302 (2015).

[61] V. Olevano, L. Reining, and F. Sottile, http://dp-code.org.

[62] L. Reining, V. Olevano, F. Sottile, S. Albrecht, and G. Onida, http://www.bethe-salpeter.org.

[63] J. Cuffe, O. Ristow, E. Chávez, A. Shchepetov, P.-O. Chapuis, F. Alzina, M. Hettich, M. Prunnila, J. Ahopelto, T. Dekorsy, and C. M. Sotomayor Torres, Phys. Rev. Lett. **110**, 095503 (2013).

[64] H. M. Lawler, A. Steigerwald, J. Gregory, H. Krzyzanowska, and N. H. Tolk, Mater. Res. Express **1**, 025701 (2014).